Optical and Quantum Electronics (2023) 55:881
https://doi.org/10.1007/s11082-023-05172-2

# Theoretical analysis of a refractive index sensor based on a photonic crystal fiber with a rectangular core

**Abdulkarem H. M. Almawgani[1] · Dana N. Alhamss[2] · Sofyan A. Taya[2] · Ayman Taher Hindi[1] · Anurag Upadhyay[3] · Shivam Singh[4] · Ilhami Colak[5] · Amrindra Pal[6] · Shobhit K. Patel[7]**

Received: 2 May 2023 / Accepted: 10 July 2023


**Abstract**
In this study, a photonic crystal fiber (PCF) sensor is proposed for refractometric sensing. The proposed PCF sensor includes a single rectangular core and 32 rectangular air holes in the cladding region that have the same width and height as the core rectangle. The fiber substance used is Zeonex. The finite element-based COMSOL 5.6 program is used to numerically analyze the model. The simulation confirms the suggested PCF capability to identify the analyte samples with extremely high sensitivity. A frequency range of 1.5–3.0 THz was adopted. At an operating frequency of 2.8 THz, many performance metrics are calculated. Extremely low effective area ($6.3575\times10^{4}$ μm$^2$), effective material loss (0.00222 cm$^{-1}$) and confinement loss ($0.52772\times10^{-14}$) have been obtained with the proposed sensor. Extremely high-power factor (98.128%), birefringence ($3.3\times10^{-3}$), numerical aperture (0.23319) and relative sensitivity (98.876%) have been also obtained with the current PCF sensor. Moreover, the fabrication possibility of the proposed sensor is further assured by the PCF design's simplicity.

**Keywords** Photonic crystal fiber · Refractometric sensor · Relative sensitivity · Confinement loss · Effective material loss

✉ Sofyan A. Taya
staya@iugaza.edu.ps

[1] Electrical Engineering Department, College of Engineering, Najran University, Najran, Kingdom of Saudi Arabia

[2] Physics Department, Islamic University of Gaza, P.O. Box 108, Gaza, Palestine

[3] Department of Applied Science and Humanities, Rajkiya Engineering College, Azamgarh, U.P., India

[4] Department of Electronics and Communication Engineering, ABES Engineering College, Ghaziabad, U.P., India

[5] Department of Electrical and Electronics Engineering, Nisantasi University, Istanbul, Turkey

[6] Department of EECE, School of Engineering and Technology, DIT University, Dehradun, Uttarakhand 248009, India

[7] Department of Computer Engineering, Marwadi University, Rajkot 360003, India

Published online: 23 July 2023

## 1 Introduction

For optical data processing (ODPG) applications, photonic crystals (PHCs) have become more attractive. Recently, PHCs have become one of the most crucial platforms for developing ODPG applications and making them affordable (Singh et al. 2020). This is performed in comparison to well-known photonic-based technologies such as modulators employed in optical networks (Mohammed and Mansi 2019), optical communication (El-Wakeel 2016), Mach–Zehnder interferometer (Mohammed et al. 2014), fibre Bragg grating (Mohammed et al. 2018) and semiconductor optical amplifiers (Shehata and Mohammed 2016). The field of PHCs is promising due to many properties including long-range monitoring, fast response, safety in highly flammable environments, immunity to electromagnetic interference, safety in highly flammable environments, and immunity to electromagnetic interference (Zhang et al. 2015). Structural design flexibility, low power consumption, and high sensitivity are further merits (Fegadolli et al. 2013). Because of these properties, a PHC is extensively used in a number of ODPG technologies as coupler (Sharifi et al. 2017), resonator (Sun et al. 2020), optical modulators (Li et al. 2020), channel drop filters (Taya et al. 2021; Almawgani et al. 2022), switches (Rajasekar et al. 2019), oscillators (Marty et al. 2021), adders (Karkhanehchi et al. 2017), logic gates (Mostafa et al. 2019), and sensors (Shaheen and Taya 2017; Taya and Shaheen 2018). Among various photonic-based sensing approaches, PHC-based sensors have recently been considered a promising technology. PHCs have been applied in the last ten years to provide cost-effective, accurate and real-life photonic-based sensors. A direct application that makes use of PHC benefits in optical fibers is photonic crystal fiber (PCF). PCFs are receiving a lot of attention from optical scientists due to their diverse capabilities. The main aspect of a PCF as an optical waveguide is characterized by their revolutionary methodology for light propagation (Habib et al. 2021). PCFs are preferred to alternative optical channels because of their compact size, durability, inexpensive cost and high tensile strength (Habib et al. 2021). Additional advantages for a PCF include single-mode propagation, design flexibility, propagation in solid core and air, controllable birefringence, and high confinement (Dash and Jha 2014). PCF can be used in numerous sensing applications in addition to offering electromagnetic signal propagation interactions with liquids and gases. For that reason, a variety of PCFs have been proposed and demonstrated as temperature sensors (Liu et al. 2018), chemical sensors (Rahaman et al. 2021), salinity sensors (Vigneswaran et al. 2018), blood component sensors (Hossain and Podder 2019), and pressure sensors (Chen et al. 2011).

The terahertz radiation band has received significant interest from the scientific community in recent years (O'Hara et al. 2019). Terahertz emission can be transmitted across PCFs and causes no risk to the health of humans (Habib et al. 2021). As a result, terahertz-based optical fiber-based sensors have been suggested and employed in a variety of real-world applications. A wide variety of PCF-based biological, chemical and biomedical sensors are designed, tested, and occasionally manufactured based on the PCF merits listed above. Examples include the detection of glucose concentration (Thenmozhi et al. 2017), blood components (Hossain and Podder 2019), protein (Islam et al. 2021), malaria (Shafkat et al. 2021), and cancer cells (Eid et al. 2021; Bulbul et al. 2020a). The most crucial PCF sensing characteristics, also known as performance evaluation criteria, are confinement loss (*CL*), relative sensitivity (*RS*), operating frequency, effective material loss (*EML*), numerical aperture (*NA*), effective area ($A_{\text{eff}}$), and fabrication feasibility with the available technology.

Through this effort, a significant attempt is made to satisfy the majority of the aforementioned standards. In this work, a PCF configuration is proposed and simulated as a refractometric sensor of three samples: S1, S2 and S3 of refractive indices of 1.333, 1.422 and 1.430, respectively. The most significant performance evaluation criteria such as confinement loss, relative sensitivity, effective area, numerical aperture, and effective material loss, are calculated. We have also compared the proposed design with similar PCF-based sensors to verify its uniqueness. The manuscript is organized as follows: Sect. 2 presents the design and fabrication feasibility of the proposed PCF configuration. The performance evaluation criteria for the proposed sensor are outlined in Sect. 3. Section 4 presents the findings, numerical results and sensing characteristics. In Sect. 5, a summary of key values for the proposed sensor performance is presented.

## 2 Sensor model design and fabrication feasibilities

Figure 1 shows a cross-sectional view of the proposed PCF sensor. The most widely used backgrounds for terahertz-based PCFs are TOPAS, Silica, Zeonex and Teflon because of their superior properties and lower absorption losses compared to other optical materials

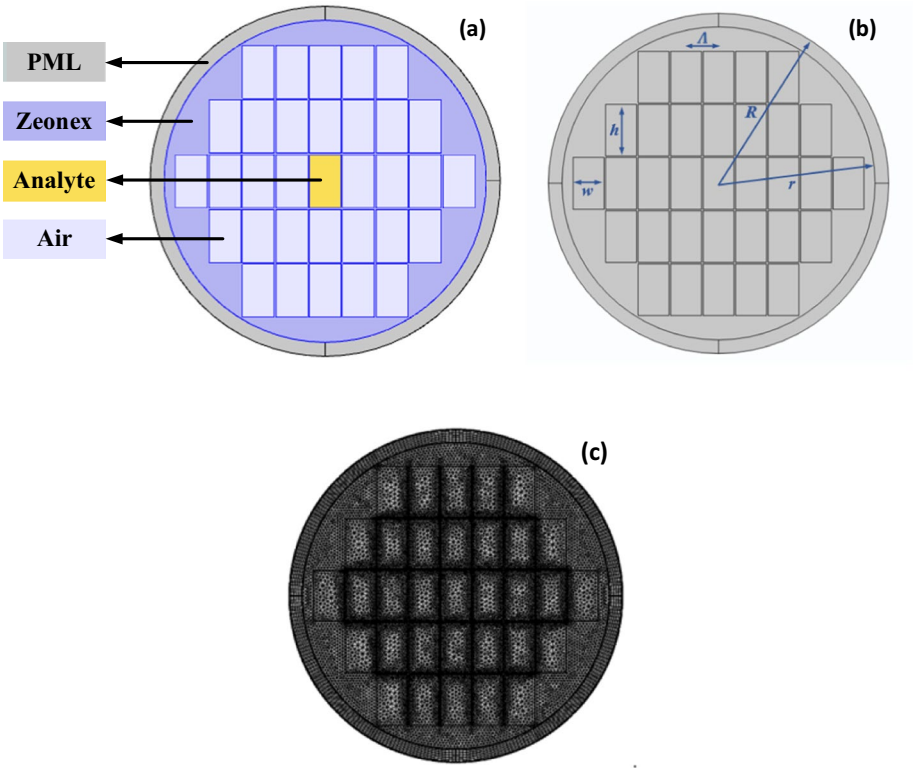


**Fig. 1** **a** Cross-sectional of the proposed PCF sensor with the yellow rectangle is the core layer. **b** Schematic diagram of the proposed PCF showing the dimensions. Here we have $w = 300\mu m$, $h = 500\mu m$, $\Lambda = 315\mu m$, $R = 1650\mu m$, $r = 1518\mu m$. **c** Meshing output which has 26,670 domain elements and 3018 boundary elements

(Habib et al. 2021). Zeonex offers excellent optical stability after exposure to heat and humidity, higher glass transition temperature, good transparency, restricted water absorption, and a minimum absorption loss of 0.2 $cm^{-1}$. It was therefore selected as the sensor's background (Islam et al. 2018). It has a refractive index (RI) of 1.53. It is characterized by low dispersion in the terahertz range. The proposed PCF structure has a rectangular core as well as rectangular air holes constituting the cladding region. COMSOL Multiphysics software (version 5.6) is used to design and simulate the proposed sensor structure. The finite element method is employed in analyzing the optical properties of the structure. Compared to other well-known numerical approaches, COMSOL is the most efficient (Dickinson et al. 2014). At first, an arbitrary PCF model is designed. Then materials are assigned in both the core and cladding regions. Initializing the boundary conditions, mesh setup is accomplished. The solutions to the partial differential equations are performed to extract performance metrics. These metrics are analyzed and the steps are repeated until standard results are attained. We have introduced the three samples (S1, S2 and S3) as analytes in the core region. The total fiber radius is taken as 1650 µm. For boundary conditions, the perfectly matched layer (PML) has a thickness of 132 µm. Here, the PML is used to absorb the electromagnetic signal propagating towards the surface.

In Fig. 1a, the yellow rectangle shows the core area where the analyte is to be injected. Figure 1b gives a detailed view of the structure of the proposed sensor along with geometrical characteristics. The width (w) and height (h) are 300 and 500 µm, respectively. The cladding region has 32 rectangular air holes. The width and height of the cladding rectangles are the same as the core rectangle. The pitch (separation between two consecutive rectangles) is 15 µm. The separation between the centers of two adjacent rectangles is $\Lambda =$ 315 µm. A normal mesh is selected to analyze the proposed PCF-based sensor. This mesh is found to have 26,670 domain elements and 3018 boundary elements. Figure 1c shows the meshing output.

The light propagation through the three analytes is illustrated in Fig. 2 in the $x$ and $y$ directions at an operating frequency $f = 2.8$ THz. Loss is minimal since just a tiny fraction of the light travels outside the core area. The maximum amount of light confinement is shown in the red area. The intensity gradually decreases towards the boundary of the core. The red arrow indicates the direction in which light travels.

The fabrication capabilities of any sensor play a key role in determining its reliability. Scientists strive to keep their designs as simple as possible to maintain fabrication capability without any damage. Extrusion (Shofner et al. 2003), 3D printing (LuO et al. 2020), stack and draw (Ishida et al. 2013), capillary stacking (Atakaramians et al. 2009) and Sol-gel (El Hamzaoui et al. 2012) are only a few of the commercially available fiber fabrication methods used to make PCF sensors today. As the proposed PCF sensor incorporates rectangular air holes, the aforementioned technologies, particularly the extrusion and 3D-printing techniques, ensure that the proposed sensor can be constructed.

## 3 Method of analysis

The problem is divided into three conditions named main structure, main structure $-2\%$, and main structure $+2\%$. To obtain these conditions we have altered the core width by $\pm 2\%$. For the main structure condition, the width and height of the core are chosen as 300 and 500 µm, respectively. For the conditions of main structure $-2\%$ and main

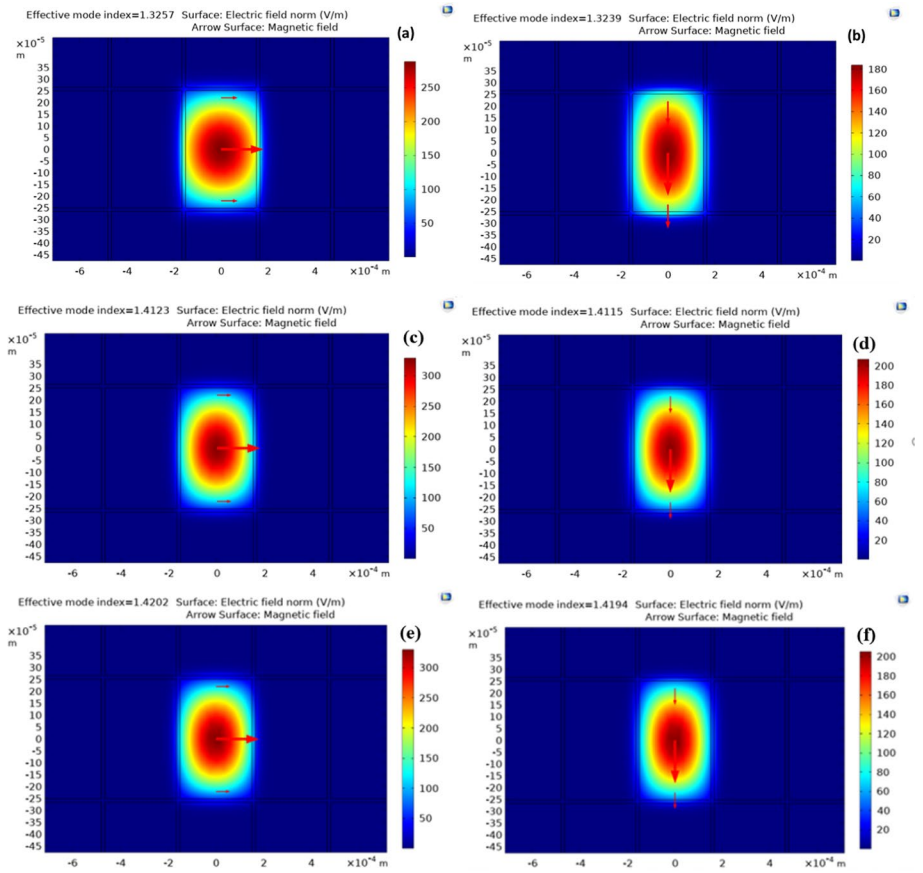


**Fig. 2** Light propagation of the proposed PCF at $f = 2.8$ THz. The analytes used here are S1 (Fig. 2a and b), S2 (Fig. 2c and d) and S3 (Fig. 2e and f). The x- and y- polarizations are shown in Fig. (2a, c and e) and (b, d and f), respectively

structure + 2%, the height remains unchanged and the width changes and takes the values of 294 µm for main structure − 2% and 306 µm for main structure + 2%.

Different assessment metrics parameters should be employed to analyze the PCF sensor performance in order to determine how well the suggested PCF sensor will detect the samples and how it can match the early detection requirements that were previously mentioned. The following parameters are regarded as characteristic of a PCF sensor applications: confinement loss (*CL*), relative sensitivity (*RS*), operating frequency, effective material loss (*EML*), numerical aperture (*NA*), effective area ($A_{\text{eff}}$), and fabrication capability with the available technology. These parameters efficiently affect the performance of a PCF sensor. The incident light must propagate primarily in the core region and be tightly restricted through the core for PCF-based sensors. Relative sensitivity is regarded as the most crucial property.

The power factor (PF), which is used to measure the light extent associated with the analytes in the core, has a substantial impact on the relative sensitivity of the PCF sensor. It is calculated as

$$PF = \frac{\int\limits_{analyte} Re\{E_x H_y - H_x E_y\} dxdy}{\int\limits_{total} Re\{E_x H_y - H_x E_y\} dxdy}, \% \tag{1}$$

$E_i$ and $H_i$ are the electric and magnetic field components in the $i$ direction. The amount of light propagating in the core and total cross-sectional regions are represented by the numerator and denominator, respectively.

The following equation is used to determine the relative sensitivity (*RS*) to an analyte when $n_r$ and $n_{eff}$ are the analyte and the effective modal RI.

$$RS = \frac{n_r}{n_{eff}} PF, \% \tag{2}$$

Birefringence is the term used to describe the asymmetry between the cladding and core region organization. It is regarded as an optical characteristic of the fiber material. The birefringence can be impacted by polarization and light propagation. The birefringence is given by the following equation when the RIs of the fiber in the $x$ and $y$ polarizations are described by $n_{eff}^x$ and$n_{eff}^y$

$$Birefringence = \left| Re\{n_{eff}^x - n_{eff}^y\} \right| \tag{3}$$

Light may occasionally propagate out from the analyte in the core region, depending on the electric field. The region where analyte sensing is most effective is known as the effective area ($A_{\text{eff}}$). A high-power density in the zone can be created by a lower $A_{\text{eff}}$ with a significant nonlinear effect.

$$A_{\text{eff}} = \frac{\left(\int |E^2| dxdy\right)^2}{\int |E^4| dxdy}, \mu m^2 \tag{4}$$

The numerical aperture (*NA*) is the largest permissible angle of incidence of injected light. It depends on $A_{\text{eff}}$, light speed (c), and operation frequency (*f*). It is believed that it will have a higher value because it measures how well a fiber can confine light. It is given by

$$NA = (1 + \pi f^2 A_{\text{eff}} / c^2)^{-1/2} \tag{5}$$

Confinement loss (*CL*) is the loss that results from the optical confinement decreasing due to the cladding-core structure of the PCF. The amount of light that is collected by the air gaps of the cladding area serves as a measure of this loss. When the *CL* is lower, the sensor quality will be higher. When $k_0 = 2\pi / \lambda$, $\lambda$ is the light wavelength, the *CL* is defined as

$$CL = 8.686 \times k_0 \times Imginary\left(n_{eff}\right) \times 10^{-2}, \text{cm}^{-1} \tag{6}$$

where $Imginary\left(n_{eff}\right)$ gives the imaginary part of the modal RI.

Effective material loss (*EML*), which the background substance can cause in considerable amounts, can be reduced by reducing the amount of background substance. It is given by

$$EML = \frac{\sqrt{\frac{\epsilon_0}{\mu_0}} \int_{mat} n_{mat}\alpha_{mat}|E|^2 dA}{\left|\int_{all} \frac{1}{2}(E \times H^*)z dA\right|}, \text{cm}^{-1} \tag{7}$$

where $n_{mat}$ and $\alpha_{mat}$ stand for the RI and bulk absorption parameter ($cm^{-1}$) for the material fiber, respectively. $\mu_0$ and $\epsilon_0$ symbolize the permeability and permittivity of free space. Table 1 lists all the variables that were used in the simulation.

## 4 Simulation results

The operating frequency region is considered 1.5–3 THz. The main aim of the current work is to detect three samples (S1, S2 and S3). Several optical parameters, including birefringence, effective area, numerical aperture, effective material loss, confinement loss, power factor, and relative sensitivity are explored for determining the effectiveness of our proposed PCF sensor. Both of the polarization directions (x- and y-polarizations) will be considered.

The aforementioned optical parameters are all dependent on the effective mode index. Figure 3 shows the effective mode index variation of the PCF for both polarization directions ($x$ and $y$) in the 1.5–3 THz frequency range. Figure 3a, c, e and b, d, f show the effective mode index of the PCF when S1, S2 and S3 are used as analytes in the x-polarized Fig. 3a, c, e and y- polarized Fig. 3b, d, f, respectively. Generally, the effective mode index increases as the frequency increases for all analytes and all polarizations. If we consider an operating frequency of $f = 2.8$ THz, the effective mode index of S1, S2 and S3 are 1.3257, 1.4123 and 1.4202 in the x- polarized and 1.3239, 1.4115 and 1.4194 in the y- polarized for the main structure. For main structure + 2%, the effective mode index of S1, S2 and S3 are 1.3242, 1.4119 and 1.4199 in the x- polarized and 1.3233, 1.4112 and 1.3281 in the

**Table 1** The parameters used for the PCF.

| | |
|---|---|
| The radius of PCF (R) | 1650 µm |
| PML | 132 µm |
| Pitch (p) | 15 µm |
| $w_{cladding}$ | 300 µm |
| $h_{cladding}$ | 500 µm |
| $w_{core}$ (main structure) | 300 µm |
| $h_{core}$ (main structure) | 500 µm |
| $w_{core}$ (main structure − 2%) | 294 µm |
| $h_{core}$ (main structure − 2%) | 500 µm |
| $w_{core}$ (main structure + 2%) | 306 µm |
| $h_{core}$ (main structure + 2%) | 500 µm |
| $n_{Zeonex}$ | 1.53 Bulbul et al. (2020a) |
| $\alpha_{Zeonex}$ | 0.2$cm^{-1}$ Islam et al. (2018) |
| $n_{S1}$ | 1.333 Taya et al. (2022) |
| $n_{S2}$ | 1.422 Taya et al. (2022) |
| $n_{S3}$ | 1.430 Taya et al. (2022) |

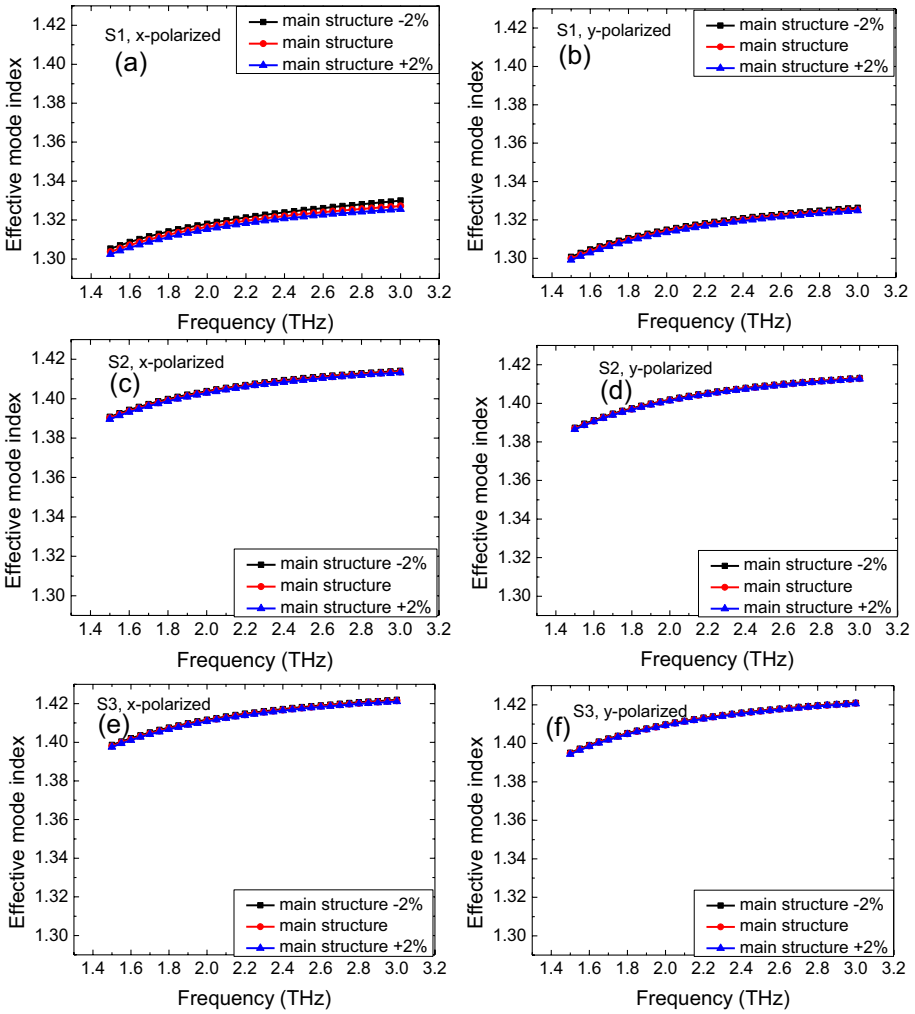


**Fig. 3** Effective mode index of the PCF structure as a function of frequency. The analytes used here are S1 (Fig. 3a and b), S2 (Fig. 3c and d) and S3 (Fig. 3e and f). The x- and y- polarizations are shown in Fig. (3a, c and e) and (b, d and f), respectively. Different colors correspond to different geometrical configurations as shown in the legends

y- polarized, respectively. For main structure $-2\%$, the effective mode index of S1, S2 and S3 are 1.3281, 1.4129 and 1.4207 in the x- polarized and 1.3248, 1.4118 and 1.4197 in the y- polarized, respectively.

When the frequency increases, the wavelength decreases, and the effective mode index tends to increase in a PCF. This behavior can be attributed to the dispersion properties of the PCF structure. Dispersion refers to the dependence of the refractive index on the wavelength or frequency of light. In PCF, different modes experience different levels of dispersion due to the variation in the effective refractive index across the operating frequency range.

Table 2 reports the effective mode index at an operating frequency of 2.8 THz for the proposed PCF sensor at different geometrical configurations and polarizations. It is clear that the effective mode index values in all cases are relatively close to the refractive indices of the analyte samples. This is a good indicator for sensor applications which can lead to extremely high sensitivity. Table 2 also shows that as the refractive index of the analyte increases, the effective mode index increases in all polarizations and PCF geometries.

Figure 4 shows the birefringence of the proposed PCF for the analytes S1 (Fig. 4a), S2 (Fig. 4b) and S3 (Fig. 4c). In most cases, the birefringence decreases as the frequency increases. At an operating frequency of 2.8 THz, the birefringence values of S1, S2 and S3 are 0.0018, 0.0008 and 0.0008, respectively for the main structure. For the main structure + 2%, the birefringence of S1, S2 and S3 are respectively given as 0.0009, 0.0007 and 0.0007. For the main structure − 2% configurations, the birefringence of S1, S2 and S3 are 0.0033, 0.0011 and 0.001, respectively. It's important to note that the relationship between frequency and birefringence in a PCF can vary depending on the specific PCF design, structural parameters, and operating conditions. Therefore, while a decrease in birefringence with increasing frequency is observed in some PCF designs, it may not hold true for all cases.

Figure 5 illustrates the effective area in $\mu m^2$ of the proposed PCF for the analytes of S1, S2 and S3 in the x-polarization (Fig. 5a, c, e) and y-polarization (Fig. 5b, d, f). The effective area of S1, S2 and S3 are 87,761, 93,928 and 93,880 $\mu m^2$ in the x-polarization and 83,635, 90,924 and 91,240 $\mu m^2$ in the y- polarization for the main structure. For the second geometrical configuration of main structure + 2%, the effective area of S1, S2 and S3 are 81,290, 91,725 and 91,940 $\mu m^2$ in the x- polarization and 99,811, 94,950 and 94,658 $\mu m^2$ in the y- polarization, respectively. For main structure − 2%, the effective

**Table 2** Effective mode index at an operating frequency of 2.8 THz.

| Analyte | Polarizations | PCF structure | Effective mode index |
|---|---|---|---|
| S1 | x-polarization | Main structure − 2% | 1.3281 |
| | | Main structure | 1.3257 |
| | | Main structure + 2% | 1.3242 |
| | y-polarization | Main structure − 2% | 1.3248 |
| | | Main structure | 1.3239 |
| | | Main structure + 2% | 1.3233 |
| S2 | x-polarization | Main structure − 2% | 1.4129 |
| | | Main structure | 1.4123 |
| | | Main structure + 2% | 1.4119 |
| | y-polarization | Main structure − 2% | 1.4118 |
| | | Main structure | 1.4115 |
| | | Main structure + 2% | 1.4112 |
| S3 | x-polarization | Main structure − 2% | 1.4207 |
| | | Main structure | 1.4202 |
| | | Main structure + 2% | 1.4199 |
| | y-polarization | Main structure − 2% | 1.4197 |
| | | Main structure | 1.4194 |
| | | Main structure + 2% | 1.3281 |

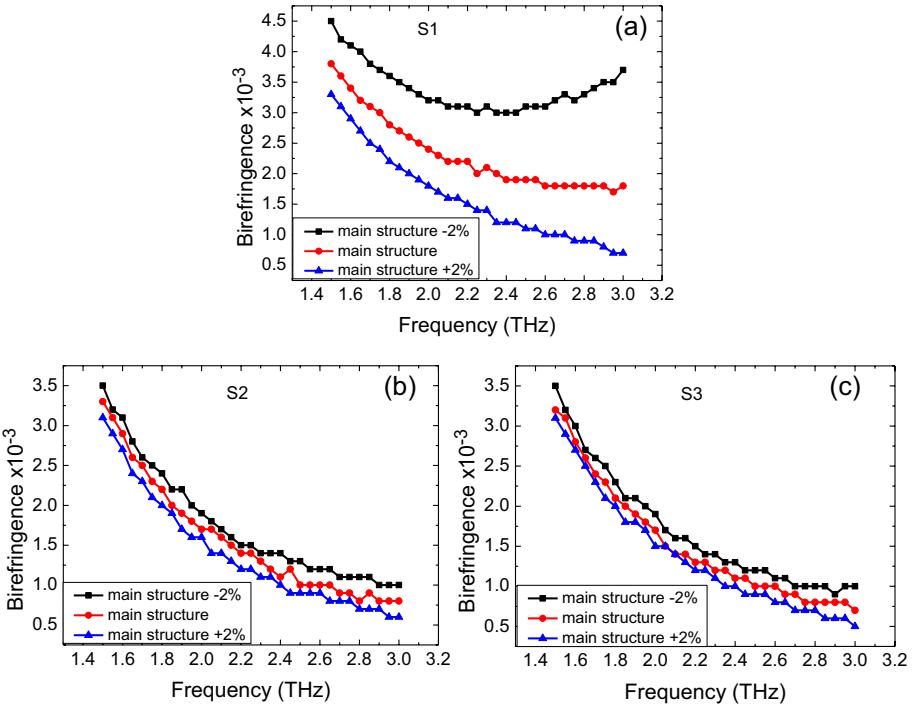


**Fig. 4** Birefringence for **a** S1, **b** S2, and **c** S3, at main structure −2%, main structure, and main structure+2% cases

area of S1, S2 and S3 are 96,595, 96,882 and 96,461 μm$^2$ in the x- polarization and 63,575, 84,393, 85,618 μm$^2$in the y- polarization, respectively.

The effective area of a PCF decreases as the frequency increases. At higher frequencies (shorter wavelengths), the dispersion properties of a PCF can cause the effective mode to be more tightly confined within the core region of the fiber. This tighter confinement leads to a decrease in the effective area of the mode.

Table 3 presents the effective area of the proposed PCF for different analytes and geometries. For a PCF, the effective area should be as low as possible to have an efficient sensor. As can be seen, the effective area, for x-polarization, decreases when the PCF shape changes from main structure −2% case to main structure ans then to main structure+2%, respectively. This means that the main structure+2% is recommended for x-polarization. The situation is different for y-polarization as the main structure −2% geometry is preferred since it corresponds to the lowest effective area.

Numerical aperture as a function of frequency is illustrated in Fig. 6 for the three analytes in x-polarization (Fig. 6a, c, e) and y-polarization (Fig. 6b, d, f). In x-polarized, the numerical aperture of S1, S2 and S3 samples are 0.19998, 0.19356 and 0.1936, respectively, whereas in the y-polarized it is given by 0.20465, 0.19661 and 0.19628, respectively, for the main structure. When we consider the main structure+2%, the numerical aperture of S1, S2 and S3 are 0.20746, 0.19578 and 0.19556 in the x-polarized and 0.18797, 0.19255 and 0.19284 in the y-polarized, respectively. For the main structure

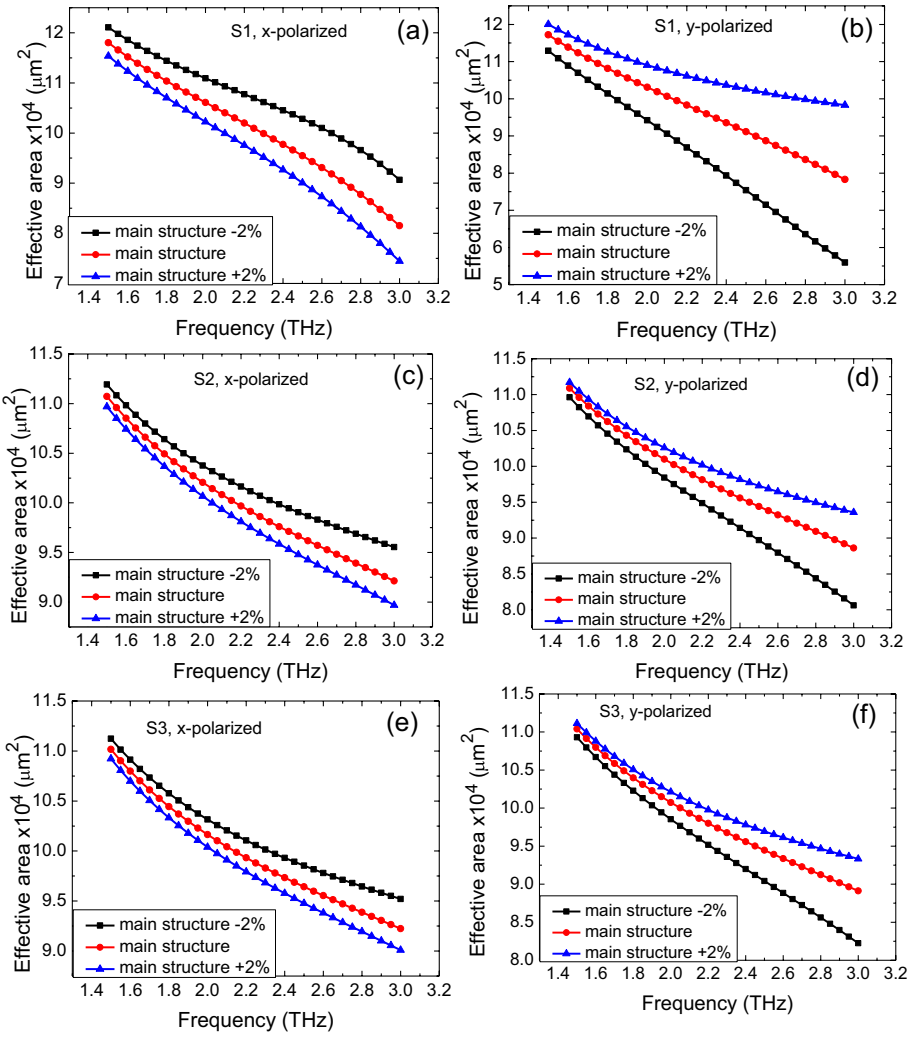


**Fig. 5** Effective area (μm$^2$) of the PCF structure as a function of frequency. The analytes used here are S1 (Fig. 5a and b), S2 (Fig. 5c and d) and S3 (Fig. 5e and f). The x- and y- polarizations are shown in Fig. (5a, c and e) and (b, d and f), respectively. Different colors correspond to different geometrical configurations as shown in the legends

−2%, the numerical aperture of S1, S2 and S3 are 0.19097, 0.19069 and 0.19109 in the x-polarized and 0.23319, 0.20377 and 0.20237 in the y-polarized, respectively.

The numerical aperture of a PCF decreases as the frequency increases. At higher frequencies (shorter wavelengths), the dispersion properties of PCF can cause the light to be more tightly confined within the core region of the fiber. This tighter confinement leads to a narrower angular range of accepted light rays, resulting in a decrease in the numerical aperture.

Effective material loss as a function of the frequency is illustrated in Fig. 7 for the three analytes in x-polarization (Fig. 7 (a, c, e)) and y-polarization (Fig. 7b, d, f). The effective

**Table 3** Effective area at an operating frequency of 2.8 THz.

| Analyte | Polarizations | PCF structure | Effectivearea $\times 10^4 (\mu m^2)$ ($f = 2.8$ THz) |
|---|---|---|---|
| S1 | x-polarization | Main structure − 2% | 9.6595 |
| | | Main structure | 8.7761 |
| | | Main structure + 2% | 8.129 |
| | y-polarization | Main structure − 2% | 6.3575 |
| | | Main structure | 8.3635 |
| | | Main structure + 2% | 9.9811 |
| S2 | x-polarization | Main structure − 2% | 9.6882 |
| | | Main structure | 9.3928 |
| | | Main structure + 2% | 9.1725 |
| | y-polarization | Main structure − 2% | 8.4393 |
| | | Main structure | 9.0924 |
| | | Main structure + 2% | 9.495 |
| S3 | x-polarization | Main structure − 2% | 9.6461 |
| | | Main structure | 9.388 |
| | | Main structure + 2% | 9.194 |
| | y-polarization | Main structure − 2% | 8.5618 |
| | | Main structure | 9.124 |
| | | Main structure + 2% | 9.4658 |

material loss of S1, S2 and S3 are 0.0162, 0.00628 and 0.00585 $cm^{-1}$ in the x-polarized and 0.00831, 0.003 and 0.0028 $cm^{-1}$ in the y-polarized for main structure, respectively. For main structure + 2%, the effective material loss of S1, S2 and S3 are 0.00846, 0.00394 and 0.00371 $cm^{-1}$ in the x-polarized and 0.00727, 0.00239 and 0.00222 $cm^{-1}$ in the y-polarized, respectively. For main structure − 2%, the effective material loss of S1, S2 and S3 are 0.03093, 0.0098 and 0.009 in the x-polarized and 0.01013, 0.00396 and 0.00371 $cm^{-1}$ in the y-polarized, respectively.

The effective material loss of an efficient PCF sensor should be as low as possible. As can be seen, as the refractive index of the analyte increases, the values of effective material loss decrease for all geometries and polarizations. It is also observed that x-polarization has effective material loss values greater than those appeared in y-polarization for all PCF structures.

Figure 8 shows the confinement loss of S1, S2 and S3 samples in the x-polarized mode (Fig. 8a, c, e) and y- polarized mode (Fig. 8b, d, f). At an operating frequency of 2.8 THz, the confinement loss of S1, S2 and S3 samples are $0.60245\times10^{-14}$, $4.3743 \times 10^{-14}$ and $0.64306 \times 10^{-14} cm^{-1}$ in the x-polarized and $0.77872\times10^{-14}$, $0.61969 \times 10^{-14}$ and $0.52772 \times 10^{-14} cm^{-1}$ in the y-polarized, respectively, for the main structure. In the case of main structure + 2% geometry, the confinement loss of S1, S2 and S3 is $0.87677\times10^{-14}$, $3.376\times10^{-14}$ and $6.2001\times10^{-14} cm^{-1}$ in the x-polarized and $3.0288\times10^{-14}$, $0.61154 \times 10^{-14}$, $6.7545 \times 10^{-14} cm^{-1}$ in the y-polarized, respectively. For main structure − 2%, the confinement loss of S1, S2 and S3 is $2.0477\times10^{-14}$, $1.1151 \times 10^{-14}$ and $3.5081 \times 10^{-14} cm^{-1}$ in the x-polarized and $1.9347\times10^{-14}$, $8.3954 \times 10^{-14}$ and $8.7792 \times 10^{-14} cm^{-1}$in the y-polarized, respectively.

The sensitivity of the PCF sensor is one of the most significant parameters that determine the sensor performance. The sensitivity value is determined by the power factor

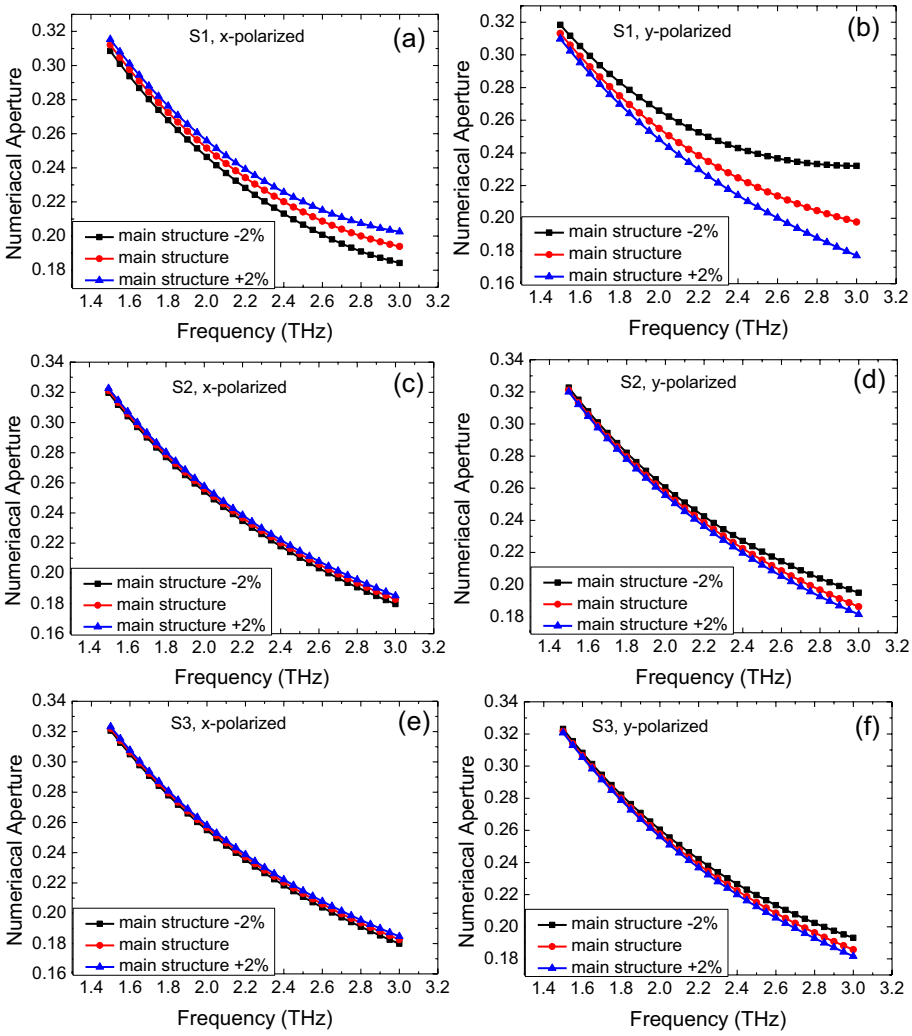


**Fig. 6** Numerical aperture of the PCF structure as a function of frequency. The analytes used here are S1 (Fig. 6a and b), S2 (Fig. 6c and d) and S3 (Fig. 6e and f). The x- and y- polarizations are shown in Fig. (6a, c and e) and (b, d and f), respectively. Different colors correspond to different geometrical configurations as shown in the legends

which is used for measuring the light extent associated with the analytes in the core. Figure 9 shows the power factor of S1, S2 and S3 in the x-polarized (Fig. 9a, c, e) and y-polarized (Fig. 9b, d, f). The power factors of S1, S2 and S3 samples are 90.067%, 96.087% and 96.35% in the x-polarized and 93.692%, 97.535% and 97.69% in the y-polarized for the main structure, respectively. For main structure + 2%, the power factors of S1, S2 and S3 are 94.114%, 97.287% and 97.442% in the x-polarized and 94.598%, 97.999% and 98.128% in the y-polarized, respectively. For main structure − 2%, the power factors of S1, S2 and S3 are 82.806%, 94.325% and 94.775% in the x-polarized and 92.212%, 96.852% and 97.05% in the y-polarized, respectively.

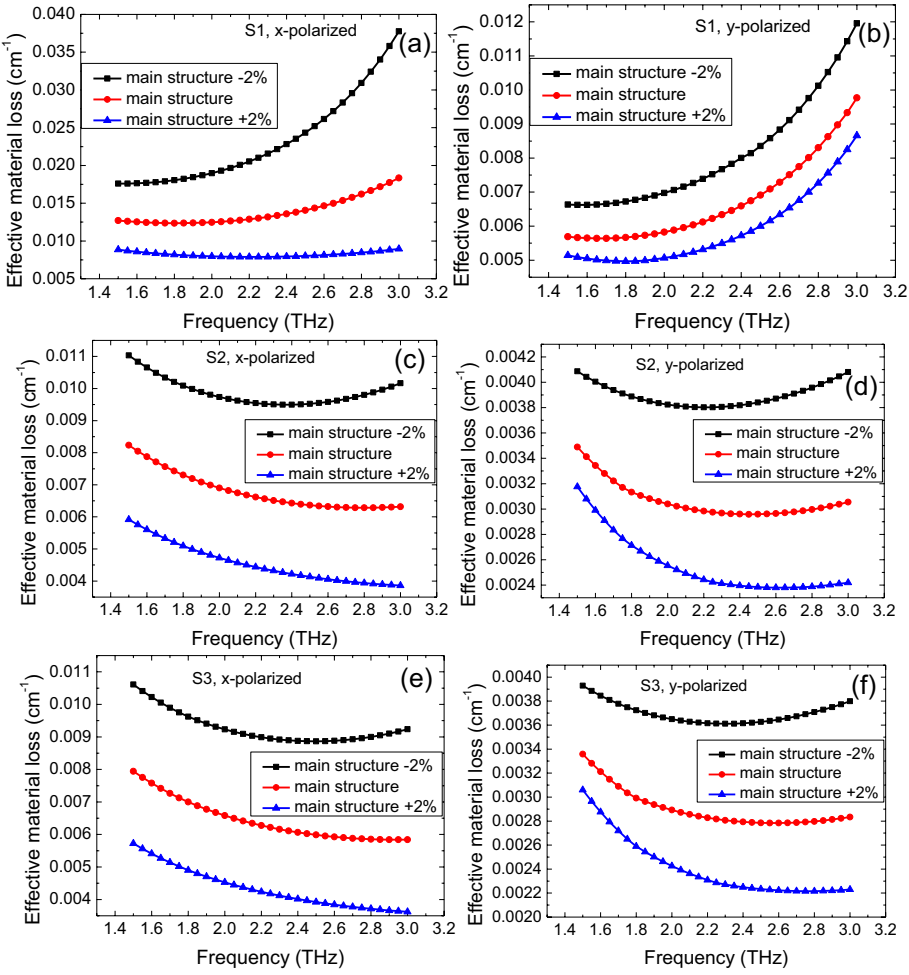


**Fig. 7** Effective material loss of the PCF structure as a function of frequency. The analytes used here are S1 (Fig. 7a and b), S2 (Fig. 7c and d) and S3 (Fig. 7e and f). The x- and y- polarizations are shown in Fig. (7a, c and e) and (b, d and f), respectively. Different colors correspond to different geometrical configurations as shown in the legends

As can be seen, the power factor can be enhanced by increasing the refractive index of the analyte sample. The case of y-polarization has higher power factors than x-polarization.

Figure 10 shows the relative sensitivity of the proposed PCF as a function of the frequency. Both polarizations are considered and the three PCF geometries are illustrated in the figure. The relative sensitivities of S1, S2 and S3 are 90.561%, 96.746% and 97.015% in the x-polarized and 94.333%, 98.263% and 98.42% in the y-polarized for main structure, respectively. For main structure + 2% geometry, the relative sensitivities of S1, S2 and S3 are 94.739%, 97.982% and 98.138% in the x-polarized and 95.288%, 98.747% and 98.876% in the y-polarized, respectively. For the geometry of main structure − 2%, the

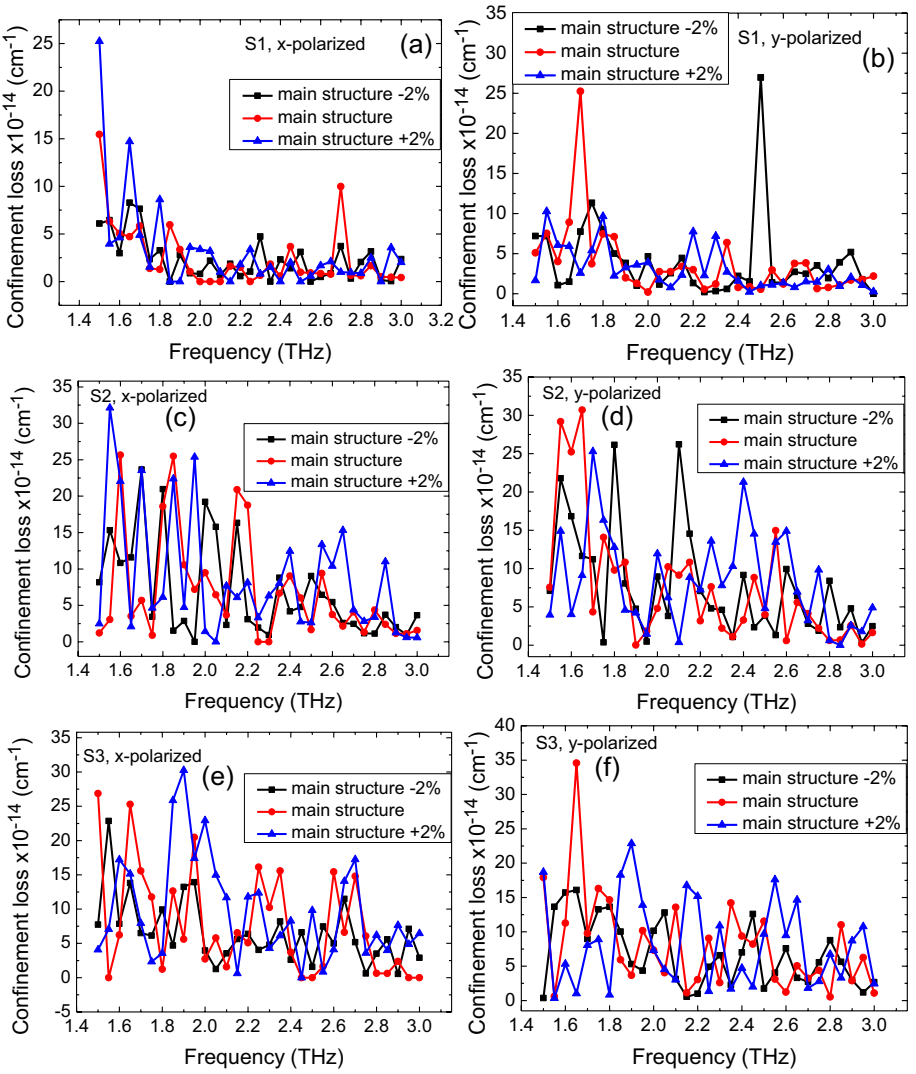


**Fig. 8** Confinement loss of the PCF structure as a function of frequency. The analytes used here are S1 (Fig. 8a and b), S2 (Fig. 8c and d) and S3 (Fig. 8e and f). The x- and y- polarizations are shown in Fig. (8a, c and e) and (b, d and f), respectively. Different colors correspond to different geometrical configurations as shown in the legends

relative sensitivities of S1, S2 and S3 are 83.11%, 94.935% and 95.397% in the x-polarized and 92.784%, 97.554% and 97.757% in the y-polarized, respectively.

Table 4 reports the relative sensitivity of the proposed PCF sensor at 2.8 THz for different geometries. As noted in the table, the relative sensitivity obtained to all analyte samples is extremely high. The proposed PCF seems promising for refractometric applications. As the analyte refractive index increases, the relative sensitivity is enhanced. When the

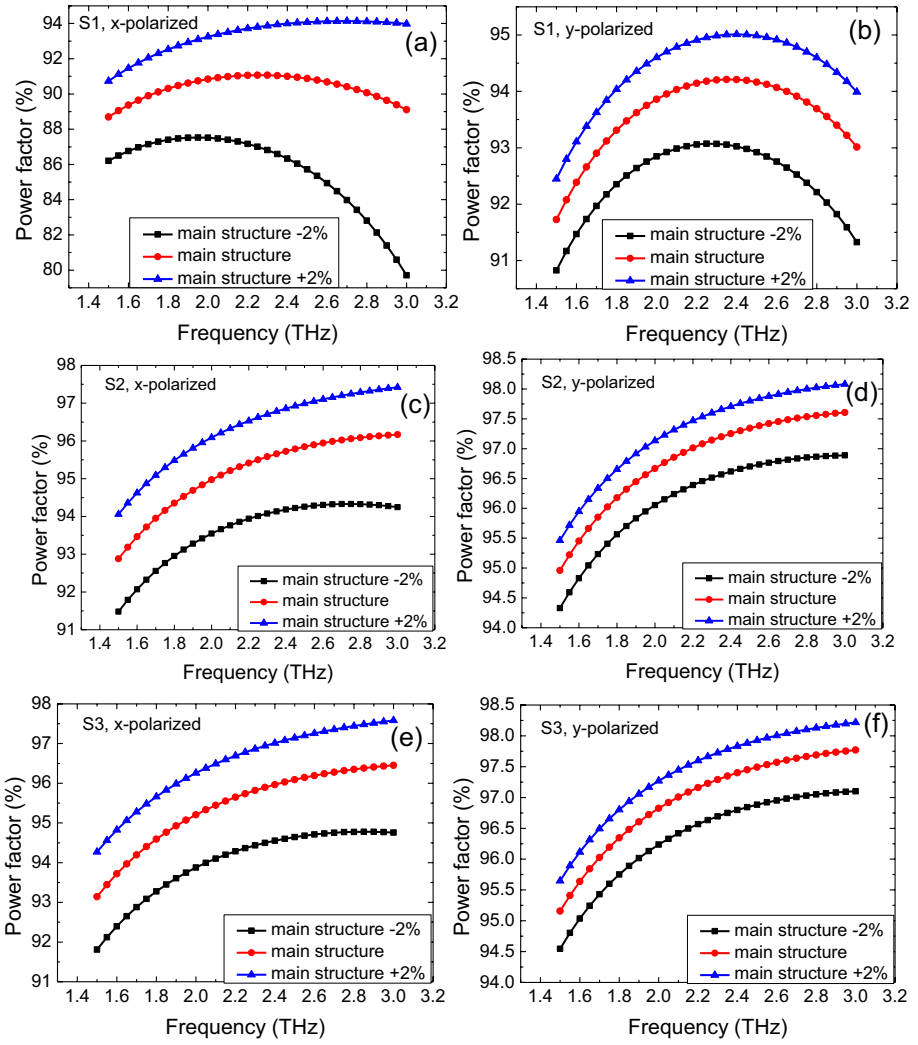


**Fig. 9** Power factor of the PCF structure as a function of frequency. The analytes used here are S1 (Fig. 9a and b), S2 (Fig. 9c and d) and S3 (Fig. 9e and f). The x- and y- polarizations are shown in Fig. (9a, c and e) and (b, d and f), respectively. Different colors correspond to different geometrical configurations as shown in the legends

y-polarization is applied to the PCF sensors, the resulting relative sensitivities are higher than those obtained when x-polarization is applied. The geometry of main structure + 2% corresponds to the highest sensitivity among all geometries considered.

The optical properties of the proposed PCF are investigated for the three configurations (main structure, main structure + 2% and main structure − 2%). The results

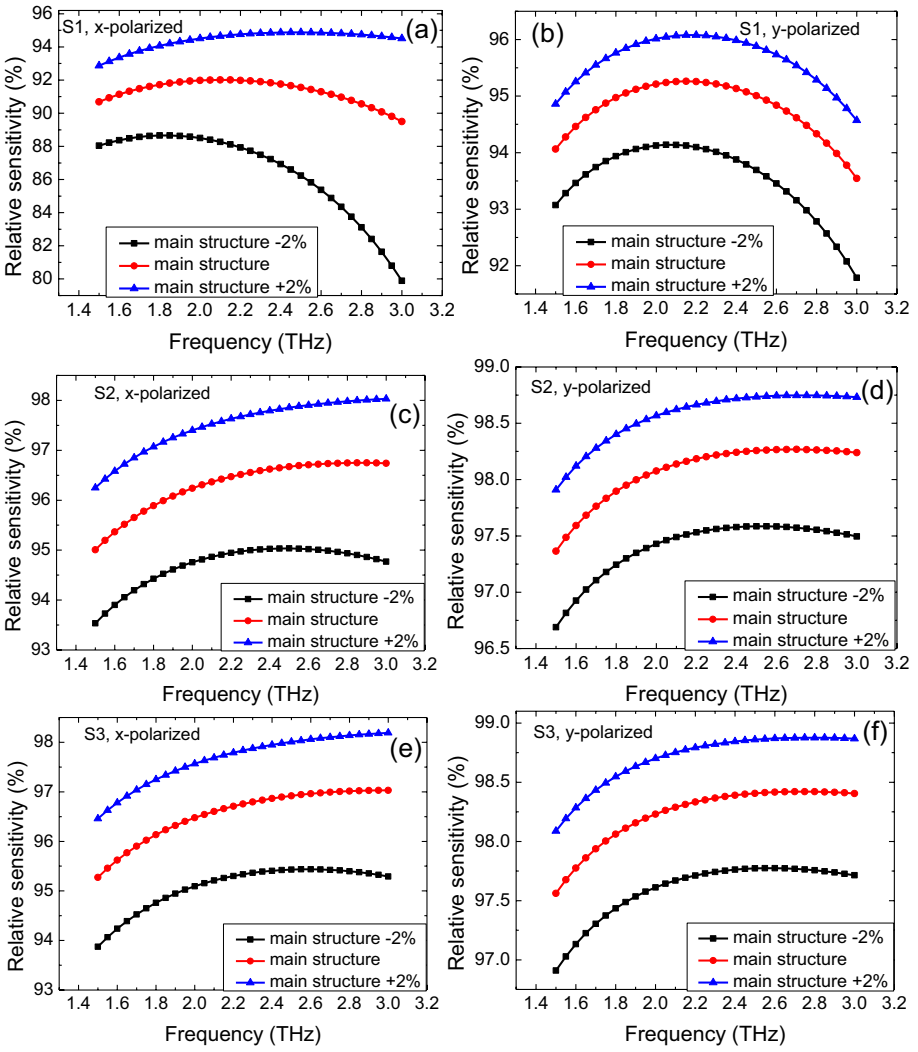


**Fig. 10** Relative sensitivity of the PCF structure as a function of frequency. The analytes used here are S1 (Fig. 10a and b), S2 (Fig. 10c and d) and S3 (Fig. 10e and f). The x- and y- polarizations are shown in Fig. (10a, c and e) and (b, d and f), respectively. Different colors correspond to different geometrical configurations as shown in the legends

demonstrate that a small change in the model structure during fabrication will not result in a significant change in the optical parameters.

The proposed PCF sensor is compared to the most recent PCF sensors in Table 5. It is clear that the proposed sensor is exceptionally effective in refractometric sensing.

**Table 4** Relative sensitivity at an operating frequency of 2.8 THz.

| Analyte | Polarizations | PCF structure | Relative sensitivity % ($f$ = 2.8 THz) |
|---|---|---|---|
| S1 | x-polarization | Main structure − 2% | 83.11 |
| | | Main structure | 90.561 |
| | | Main structure + 2% | 94.739 |
| | y-polarization | Main structure − 2% | 92.784 |
| | | Main structure | 94.333 |
| | | Main structure + 2% | 95.288 |
| S2 | x-polarization | Main structure − 2% | 94.935 |
| | | Main structure | 96.746 |
| | | Main structure + 2% | 97.982 |
| | y-polarization | Main structure − 2% | 97.554 |
| | | Main structure | 98.263 |
| | | Main structure + 2% | 98.747 |
| S3 | x-polarization | Main structure − 2% | 95.397 |
| | | Main structure | 97.015 |
| | | Main structure + 2% | 98.138 |
| | y-polarization | Main structure − 2% | 97.757 |
| | | Main structure | 98.42 |
| | | Main structure + 2% | 98.876 |

## 5 Conclusions

In this paper, we have proposed and numerically analyzed a PCF sensor for the detection of three samples. The cladding zone has 32 rectangular air holes and the PCF core is made up of a single rectangle that has the same dimensions as those of the cladding. The fiber substance used is Zeonex. Three different PCF configurations have been investigated: main structure, main structure + 2% and main structure − 2%. These configurations have been obtained by changing the core width by ± 2%. The essential optical parameters have been analyzed for each structure. An operating frequency of 2.8 THz is chosen. The effective mode index has been found close to the refractive indices of the analyte samples. This is a good sign for sensor applications which can lead to extremely high sensitivity. When the y-polarization is applied to the proposed PCF sensor and the geometry of main structure + 2% is considered, the highest-power factor (98.128%) and relative sensitivity (98.876%) were obtained. Many noteworthy findings related to the performance indicators have been found. Extremely low effective area ($6.3575 \times 10^4$ μm$^2$), effective material loss (0.00222 cm$^{-1}$) and confinement loss ($0.52772 \times 10^{-14}$) have been obtained with the proposed sensor. Extremely high birefringence ($3.3 \times 10^{-3}$) and numerical aperture (0.23319) have been also obtained with the current PCF sensor. These values indicate a promising and efficient PCF detector. The numerical results of the optical parameters show that only little modifications in the fabrication of the proposed PCF will not have a major impact on the optical parameters.

**Table 5** Performance comparison between current work and most recent published PCFs.

| Reference | Sensitivity (%) | Effective area ($\mu m^2$) | Numerical aperture | Birefringence | Confinement loss ($cm^{-1}$) | Effective material loss ($cm^{-1}$) | Frequency (THz)/ Wavelnegth (μm) | Structure type |
|---|---|---|---|---|---|---|---|---|
| Arif et al. (2019) | 41.4 | – | – | 0.00509 | $2.17\times10^{-12}$ | – | λ = 1.3 μm | PCF with elliptical core |
| Bin Murshed Leon et al. (2021) | 44.45 | – | – | 0.0027 | $6.54\times10^{-6}$ | – | λ = 1.3 μm | PCF with group of circular core with different diameters |
| Leon et al. (2020) | 49.1 | – | – | 0.008 | $5.58\times10^{-7}$ | – | λ = 1.3 μm | PCF with group of circular core with different diameters |
| Hasan et al. (2019) | 63.2 | 144,000 | – | – | $2.50\times10^{-7}$ | – | f = 1 THz | PCF with two different types of the circular core |
| Hossain et al. (2021) | 68.48 | – | – | – | $2.13\times10^{-11}$ | – | f = 1 THz | PCF with Rotated-hexa core region and Heptagonal cladding region |
| Abdullah-Al-Shafi and Sen (2020) | 77.14 | – | – | – | $2.26\times10^{-5}$ | – | f = 1 THz | PCF with Rotated-hexa core region and Octagonal cladding region |
| Mou et al. (2020) | 90 ± 1 | $5\times10^{4}$ | – | – | $10^{-16\pm1}$ | 0.02 | f = 1 THz | PCF with square core |
| Bulbul et al. (2020a) | 91.5 | 397,340 | – | – | $4.87\times10^{-11}$ | 0.004 | f = 1.8 THz | PCF with rectangular core |
| Bulbul et al. (2020b) | 92.2 | 93,754 | 0.194 | 0.001 | $6.52\times10^{-14}$ | 0.0117 | f = 2.8 THz | PCF with rectangular core |
| Iqbal et al. (2020) | 92.3 | 209,930 | - | 0.001 | $5.94\times10^{-15}$ | 0.006 | f = 2 THz | PCF with rectangular core |

**Table 5** (continued)

| Reference | Sensitivity (%) | Effective area ($\mu m^2$) | Numerical aperture | Birefringence | Confinement loss ($cm^{-1}$) | Effective material loss ($cm^{-1}$) | Frequency (THz)/ Wavelnegth (μm) | Structure type |
|---|---|---|---|---|---|---|---|---|
| Jibon et al. (2021a) | 96.50 | $1.59\times10^{5}$ | 0.225 | – | $2.68\times10^{-13}$ | 0.008 | f = 1.9 THz | PCF with square core |
| Jibon et al. (2021b) | 94.2 | $3.13\times10^{5}$ | 0.17707 | – | $1.28\times10^{-13}$ | 0.0059 | f = 1.7 THz | PCF with rectangular core |
| The proposed sensor | 98.876 | 63,575 | 0.23319 | $3.3\times10^{-3}$ | $0.52772\times10^{-14}$ | 0.00222 | f = 2.8 THz | PCF with rectangular core |

**Acknowledgements** The authors are thankful to the Deanship of Scientific Research at Najran University for funding this work under the Research Priorities and Najran Research funding program grant code (NU/NRP/SERC/12/2).

**Author contributions** The authors confirm their contribution to the paper as follows: study conception and design (DNA, SAT). Software (AHMA). Interpretation of results (AU, SS, IC). Draft manuscript preparation (AP, SKP). Writing the final version (SAT, AT Hindi). Supervision (SAT). All authors reviewed the results and approved the final version of the manuscript.

**Funding** Deanship of Scientific Research at Najran University.

**Data availability** The datasets generated during or analyzed during the current study are available from the corresponding author on reasonable request.

## Declarations

**Conflict of interest** The authors declare no competing interests.

**Consent to participate** No consent to participate is required for this study.

**Consent for Publish** No consent for publication is required for this study.

## References

Abdullah-Al-Shafi, M., Sen, S.: Design and analysis of a chemical sensing octagonal photonic crystal fiber (O-PCF) based optical sensor with high relative sensitivity for terahertz (THz) regime. Sens. Bio-Sens. Res. **29**, 100372 (2020). https://doi.org/10.1016/j.sbsr.2020.100372

Almawgani, A.H.M., Alhamss, D.N., Taya, S.A., Colak, I., Sharma, A., Alhawari, A.R.H., Patel, S.K.: The properties of a tunable terahertz filter based on a photonic crystal with a magnetized plasma defect layer. Phys. Fluids **34**(8), 082020 (2022). https://doi.org/10.1063/5.0106995

Arif, M.F.H., Hossain, M.M., Islam, N., Shah, M.K.: A nonlinear photonic crystal fiber for liquid sensing application with high birefringence and low confinement loss. Sens. Biosens. Res. **22**, 100252 (2019). https://doi.org/10.1016/j.sbsr.2018.100252

Atakaramians, S., Afshar, S., Ebendorff-Heidepriem, H., Nagel, M., Fischer, B.M., Abbott, D., et al.: THz porous fibers: design, fabrication and experimental characterization. Opt. Express **17**(16), 14053–14062 (2009). https://doi.org/10.1364/OE.17.014053

Bin Murshed Leon, M.J., Abedin, S., Kabir, M.A.: A photonic crystal fiber for liquid sensing application with high sensitivity, birefringence and low confinement loss. Sens. Int. **2**, 100061 (2021). https://doi.org/10.1016/j.sintl.2020.100061

Bulbul, A.A.-M., Hossain, M.B., Dutta, R., Hassan, M.: Zeonex-based tetra-rectangular core-photonic crystal fiber for NaCl detection. Nanosci. Nanotechnol **11**(4), 1–9 (2020). https://doi.org/10.2174/2210681210999200708141725

Bulbul, A.A.-M., Rahaman, H., Biswas, S., Hossain, M.B., Nahid, A.: Design and numerical analysis of a PCF-based bio-sensor for breast cancer cell detection in the THz regime. Sens. Bio-Sens. Res. **30**, 100388 (2020). https://doi.org/10.1016/j.sbsr.2020.100388

Chen, D., Hu, G., Chen, L.: Dual-core photonic crystal fiber for hydrostatic pressure sensing. IEEE Photonics Technol. Lett. **23**(24), 1851–1853 (2011). https://doi.org/10.1109/LPT.2011.2170194

Dash, J.N., Jha, R.: Graphene-based birefringent photonic crystal fiber sensor using surface plasmon resonance. IEEE Photonics Technol. Lett. **26**(11), 1092–1095 (2014)

Dickinson, E.J.F., Ekström, H., Fontes, E.: COMSOL multiphysics: finite element software for electrochemical analysis. A mini-review. Electrochem. Commun. **40**, 71–74 (2014). https://doi.org/10.1016/j.elecom.2013.12.020

Eid, M., Rashed, A.N.Z., Bulbul, A.A.-M., Podder, E.: Mono-rectangular core photonic crystal fiber (MRC-PCF) for skin and blood cancer detection. Plasmonics. **16**, 717–727 (2021). https://doi.org/10.1007/s11468-020-01334-0

El-Wakeel, A.S., Mohammed, N.A., Aly, M.H.: Free space optical communications system performance under atmospheric scattering and turbulence for 850 and 1550 nm operation. Appl. Opt **55**(26), 7276–7286 (2016). https://doi.org/10.1364/AO.55.007276

El Hamzaoui, H., Ouerdane, Y., Bigot, L., Bouwmans, G., Capoen, B., Boukenter, A., et al.: Sol-gel derived ionic copper-doped microstructured optical fiber: a potential selective ultraviolet radiation dosimeter. Opt. Express **20**(28), 29751–29760 (2012). https://doi.org/10.1364/OE.20.029751

Fegadolli, W.S., Oliveira, J.E.B., Almeida, V.R., Scherer, A.: Compact and low power consumption tunable photonic crystal nanobeam cavity. Opt. Express **21**(3), 3861 (2013). https://doi.org/10.1364/OE.21.003861

Habib, A., Rashed, A.N.Z., El-Hageen, H.M., Alatwi, A.M.: Extremely sensitive photonic crystal fiber–based cancer cell detector in the terahertz regime. Plasmonics **16**(4), 1297–1306 (2021)

Hasan, M.M., Sen, S., Rana, M.J., Paul, B.K., Habib, M.A., Daiyan, G.M., Ahmed, K.: Heptagonal photonic crystal fiber based chemical sensor in THz regime. In: 2019 Joint 8th International Conference on Informatics, Electronics & Vision (ICIEV) and 2019 3rd International Conference on Imaging, Vision & Pattern Recognition (icIVPR), IEEE. 40–44 (2019). https://doi.org/10.1109/ICIEV.2019.8858555

Hossain, M., Podder, E.: Design and investigation of PCF-based blood components sensor in terahertz regime. Appl. Phys. A **125**(861), 1–8 (2019). https://doi.org/10.1007/s00339-019-3164-x

Hossain, M.S., Sen, S.: Design and performance improvement of optical chemical sensor based photonic crystal fiber (PCF) in the Terahertz (THz) wave propagation. Silicon **13**(11), 3879–3887 (2021). https://doi.org/10.1007/s12633-020-00696-8

Iqbal, F., Biswas, S., Bulbul, A.A.-M., Rahaman, H., Hossain, M.B., Rahaman, M.E., Awal, M.A.: Alcohol sensing and classification using PCF-based sensor. Sens. Biosens. Res. **30**, 100384 (2020). https://doi.org/10.1016/j.sbsr.2020.100384

Ishida, I., Akamatsu, T., Wang, Z., Sasaki, Y., Takenaga, K., Matsuo, S.: Possibility of stack and draw process as fabrication technology for multi-core fiber. In: Optical Fiber Communication Conference and Exposition and National Fiber Optic Engineers Conference, pp. 1–3. IEEE (2013). https://doi.org/10.1364/OFC.2013.OTu2G.1

Islam, M., Islam, M.R., Al Naser, A.M., Anzum, F., Jaba, F.Z.: Square structured photonic crystal fiber based THz sensor design for human body protein detection. J. Comput. Electron. **20**, 377–386 (2021). https://doi.org/10.1007/s10825-020-01606-2

Islam, M.S., Sultana, J., Dinovitser, A., Ng, B.W.-H., Abbott, D.: A novel Zeonex based oligoporous-core photonic crystal fiber for polarization preserving terahertz applications. Opt. Commun. **413**(15), 242–248 (2018). https://doi.org/10.1016/j.optcom.2017.12.061

Jibon, R.H., Ahmed, M., Hasan, M.K.: Identification of detrimental chemicals of plastic products using PCF in the THz regime. Measurement: Sens. **17**, 100056 (2021). https://doi.org/10.1016/j.measen.2021.100056

Jibon, R.H., Rahaman, M.E., Alahe, M.A.: Detection of primary chemical analytes in the THz regime with photonic crystal fiber. Sens. Bio-Sens. Res. **33**, 100427 (2021). https://doi.org/10.1016/j.sbsr.2021.100427

Karkhanehchi, M.M., Parandin, F., Zahedi, A.: Design of an all optical half-adder based on 2D photonic crystals. Photonic Netw. Commun. **33**, 159–165 (2017). https://doi.org/10.1007/s11107-016-0629-0

Leon, M.J.B.M., Kabir, M.A.: Design of a liquid sensing photonic crystal fiber with high sensitivity, bireferingence and low confinement loss. Sens. Biosens. Res **28**, 1–7 (2020). https://doi.org/10.1016/j.sbsr.2020.100335

Li, M., Ling, J., He, Y., Javid, U.A., Xue, S., Lin, Q.: Lithium niobate photonic-crystal electro- optic modulator. Nat. Commun. **11**, 1–8 (2020). https://doi.org/10.1038/s41467-020-17950-7

Liu, Q., Li, S.-G., Chen, H.: Enhanced sensitivity of temperature sensor by a PCF with a defect core based on sagnac interferometer. Sens. Actuators B Chem. **254**, 636–641 (2018). https://doi.org/10.1016/j.snb.2017.07.120

Luo, Y., Canning, J., Zhang, J., Peng, G.-D.: Toward optical fibre fabrication using 3D printing technology. Opt. Fiber Technol. **58**, 102299 (2020). https://doi.org/10.1016/j.yofte.2020.102299

Marty, G., Combrié, S., Raineri, F., Rossi, A.D.: Photonic crystal optical parametric oscillator. Nat. Photonics **15**(1), 53–58 (2021). https://doi.org/10.1038/s41566-020-00737-z

Mohammed, N.A., Elnasr, A., Aly, H.S.: Analysis and design of an electro-optic $2\times2$ switch using Ti: $KNbO_3$ as a waveguide based on MZI at 1.3 μ m. Opt. Quantum Electron. **46**, 295–304 (2014). https://doi.org/10.1007/s11082-013-9760-7

Mohammed, N.A., Mansi, A.M.: Performance enhancement and capacity enlargement for a DWDMPON system utilizing an optimized cross seeding rayleigh backscattering design. Appl. Sci. **9**(21), 4520 (2019). https://doi.org/10.3390/app9214520

Mohammed, N.A., El Serafy, H.O.: Ultra-sensitive quasi-distributed temperature sensor based on an apodized fiber Bragg grating. Appl. Opt. **57**(2), 273–282 (2018). https://doi.org/10.1364/AO.57.000273

Mostafa, T.S., Mohammed, N.A., El-Rabaie, E.-S.M.: Ultra-high bit rate all-optical AND/OR logic gates based on photonic crystal with multi-wavelength simultaneous operation. J. Mod. Opt. **66**(24), 1005–1016 (2019). https://doi.org/10.1080/09500340.2019.1598587

Mou, F.A., Rahman, M.M., Islam, M.R., Bhuiyan, M.I.H.: Development of a photonic crystal fiber for THz wave guidance and environmental pollutants detection. Sens. Biosens. Res **29**, 100346 (2020). https://doi.org/10.1016/j.sbsr.2020.100346

O'Hara, J.F., Ekin, S., Choi, W., Song, I.: A perspective on terahertz next-generation wireless communications. Technologies **7**(2), 43 (2019). https://doi.org/10.3390/technologies7020043

Rahaman, M.E., Jibon, R.H., Mondal, H.S., Hossain, M.B., Bulbul, A.A.-M., Saha, R.: Design and optimization of a PCF-based chemical sensor in THz regime. Sens. Bio-Sens. Res. **32**, 100422 (2021). https://doi.org/10.1016/j.sbsr.2021.100422

Rajasekar, R., Parameshwari, K., Robinson, S.: Nano-optical switch based on photonic crystal ring resonator. Plasmonics **14**(6), 1687–1697 (2019). https://doi.org/10.1007/s11468-019-00955-4

Shafkat, A., Rashed, A.N.Z., El-Hageen, H.M., Alatwi, A.M.: Design and analysis of a single elliptical channel photonic crystal fiber sensor for potential malaria detection. J. Sol-Gel Sci. Technol **98**, 202–211 (2021). https://doi.org/10.1007/s10971-021-05490-5

Shaheen, S.A., Taya, S.A.: Propagation of p-polarized light in photonic crystal for sensor application. Chin. J. Phys **55**(2), 571–582 (2017). https://doi.org/10.1016/j.cjph.2016.12.005

Sharifi, H., Hamidi, S.M., Navi, K.: All-optical photonic crystal logic gates using nonlinear directional coupler. Photonics Nanostruct. Fundam. Appl. **27**, 55–63 (2017). https://doi.org/10.1016/j.photonics.2017.10.002

Shehata, M.I., Mohammed, N.A.: Design and optimization of novel two inputs optical logic gates (NOT, AND, OR and NOR) based on single commercial TW-SOA operating at 40 Gbit/s. Opt. Quantum Electron. **48**(6), 1–16 (2016). https://doi.org/10.1007/s11082-016-0602-2

Shofner, M.L., Rodríguez-Macías, F.J., Vaidyanathan, R., Barrera, E.V.: Single wall nanotube and vapor grown carbon fiber reinforced polymers processed by extrusion freeform fabrication. Compos. Part. A Appl. Sci. Manuf. **34**(12), 1207–1217 (2003). https://doi.org/10.1016/j.compositesa.2003.07.002

Singh, J.J., Dhawan, D., Gupta, N.: All-optical photonic crystal logic gates for optical computing: an extensive review. Opt. Eng **59**(11), 110901 (2020). https://doi.org/10.1117/1.OE.59.11.110901

Sun, F., Dong, B., Wei, J., Ma, Y., Tian, H., Lee, C.: Demonstration of mid-infrared slow light one-dimensional photonic crystal ring resonator with high-order photonic bandgap. Opt. Express **28**(21), 30736–30747 (2020). https://doi.org/10.1364/OE.392677

Taya, S.A., Abutailkh, M.A., Colak, I., Ramahi, O.M.: Modelling of three tunable multichannel filters using Ag metal as a defect layer in a photonic crystal. Opt. Quant Electron. **53**, 644 (2021). https://doi.org/10.1007/s11082-021-03307-x

Taya, S.A., Alhamss, D.N., Colak, I., et al.: Sensitivity enhancement of an optical sensor based on a binary photonic crystal for the detection of Escherichia coli by controlling the central wavelength and the angle of incidence. Opt. Quant. Electron. **54**, 127 (2022). https://doi.org/10.1007/s11082-022-03511-3

Taya, S.A., Shaheen, S.A.: Binary photonic crystal for refractometric applications (TE case). Indian J. Phys. **92**(4), 519–527 (2018). https://doi.org/10.1007/s12648-017-1130-z

Thenmozhi, H., Rajan, M.M., Devika, V., Vigneswaran, D., Ayyanar, N.: D-glucose sensor using photonic crystal fiber. Optik (Stuttg) **145**, 489–494 (2017). https://doi.org/10.1016/j.ijleo.2017.08.039

Vigneswaran, D., Ayyanar, N., Sharma, M., Sumathi, M., Rajan, M., Porsezian, K.: Salinity sensor using photonic crystal fiber. Sens. Actuators Phys. **269**, 22–28 (2018). https://doi.org/10.1016/j.sna.2017.10.052

Zhang, Y., Zhao, Y., Lv, R.: A review for optical sensors based on photonic crystal cavities. Sens. Actuators Phys. **233**, 374–389 (2015). https://doi.org/10.1016/j.sna.2015.07.025